Proceedings of the ASME 2017 International Design Engineering Technical Conferences and Computers and Information in Engineering Conference
IDETC/CIE 2017
August 6-9, 2017, Cleveland, Ohio, USA

DETC2017-68074

EXPERIMENTAL VALIDATION OF UNLUMPED MODEL AND ITS DESIGN IMPLICATIONS FOR ROTARY SERIES ELASTIC ACTUATORS

Jeong H. Yoon
University of California, Los Angeles
Los Angeles, California, USA

Daniel Sun
University of California, Los Angeles
Los Angeles, California, USA

Vidur Sanandan
University of California, Los Angeles
Los Angeles, California, USA

Dennis Hong, Ph.D.
University of California, Los Angeles
Los Angeles, California, USA

ABSTRACT

Series Elastic Actuators (SEA) have been in development for multiple decades. In spite of this, few design guidelines exist and stiffness selection for the compliant element still remains a trial-and-error process. In this paper, we experimentally validated the unlumped model first proposed by Orekhov for Rotary SEA(RSEA) and outlined a design methodology for selecting the spring stiffness based on the open loop force control bandwidth of unlumped model for series elastic actuators. We modified the unlumped model to apply to Rotary SEAs. Through experimental system identification, we demonstrated that our new unlumped model for RSEA is a valid model of actuator dynamics. Additionally, we recommended design guidelines for RSEA to achieve desired force control bandwidth based on the pure torque source assumption. An example of the design process was given and actuator performance was verified through dynamic simulations in ADAMS.

NOMENCLATURE

T torque
K spring stiffness
M motor
G gear
SC spring chassis
J inertia
b damping
N gear ratio
Mu Mutual Inductance
J_{eff} sum of reflected inertia and motor chassis inertia
b_{eff} sum of reflected damping and spring damping
ϑ angle
K_s joint stiffness
R moment arm radius
r_s spring radius
$*_m$ quantities related to motors
$*_c$ quantities related to motor chassis
$*_p$ proximal, end of the actuator closer to robot base
$*_d$ distal, the end of the actuator closer to end effector
$*_o*$ output of the motor
$*_s$ quantities associated with the spring
$*_l*$ quantities associated with the output load

1. INTRODUCTION

Endowing robots with the ability to interact harmoniously with their environment and work alongside humans has always

been one of the chief goals of robotics. As part of this attempt, compliant actuators such as Series Elastic Actuator (SEA) were devised since compliance has paramount importance in interaction between robots and environment to ensure stable contact and operational safety. Ever since Gill Pratt introduced the idea of SEA [1], researchers have been striving to improve their performance by implementing various type of mechanisms in a growing number of compliant humanoid robots. For example, electromechanical linear SEAs with ball screw reduction mechanisms [2–4] are widely used thanks to their high power efficiency, impact tolerance, and back-drivable features. SAFFiR [5], THOR [6], M2V2 [7] and Valkyrie [8] are humanoid robots that use electromechanical linear SEAs. Rotary SEAs are also widely investigated due to their compactness. RSEAs with harmonic drive reduction mechanisms [9] have been incorporated in COMAN [10], Walkman [11], Valkyrie [8], and Toro [12]. Cable driven SEAs allow remote drive of a revolute joint, and their advantages are well exploited in Roboray [13] and Flame/TUlip [14]. Further, Variable Stiffness Actuators (VSA) that adjust their stiffness based on the task that robots are given are being studied and developed. [15–18]. However, since VSAs introduce a significant amount of weight and complexity due to an additional actuator that is designed to change its stiffness, practical implementation in humanoid robots remains difficult. Therefore, we conclude that more focus should be given to develop a conventional SEA but with an improved design criteria considering the limitations imposed by the current technology in bipedal robots. Among all the benefits of compliant actuators, namely energy storage, shock absorption, and increased force control fidelity, more focus should be given to force control fidelity since accurate force control is critical for robots to stably interact with environment. In order to achieve high force fidelity, selecting the proper stiffness value is critical for a successful design, but relatively little work has been done in this regard. Orekhov [19], Robinson [20], and Paine [4] wrote papers on actuator design, but all of them focused on linear SEAs. In this research and following ones, our focus will be on establishing design criteria for Rotary SEAs based on force control bandwidth analysis.

In this paper, we extend the unlumped model presented by Orekhov to a Rotary SEA case and experimentally verify that the unlumped model is a valid representation of Rotary SEAs. We also designed a prototype Rotary SEA, simulated it in ADAMS based on the unlumped model and showed that the designed prototype can achieve a target force control frequency as long as the spring stiffness is chosen based on the unlumped model.

2. UNLUMPED MODEL VS. LUMPED MODEL

2.1 Mechanical Representation of Rotary SEA

By definition, a Series Elastic Actuator is an actuator that contains a mechanical compliance in series with the actuator. A mechanical schematic is shown in Fig. 1

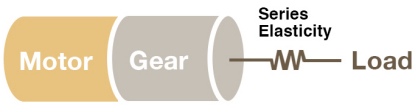

FIGURE 1. SCHEMATIC OF SERIES ELASTIC ACTUATOR

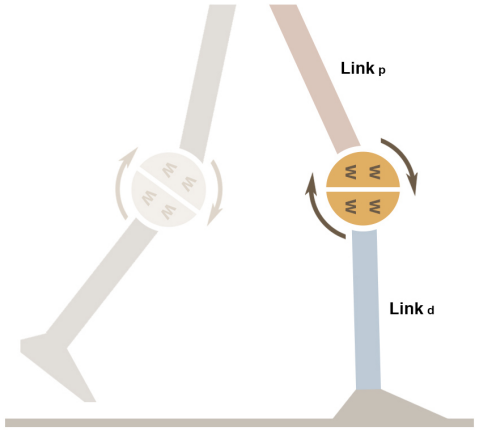

FIGURE 2. BIPEDAL WALKING ROBOT IN SINGLE SUPPORT

The traditional lumped model for series elastic actuators lumps the reflected inertia of the gears with the inertia of the actuator chassis. However, as Orekhov [19] first pointed out and Schutz followed [21], modeling the actuator as a lumped model can falsely inflate the importance of reflected inertia and can possibly lead to poor design choices.

The lumped model was considered a valid representation of the actuator for a long time because people depicted the single support phase of bipedal gait shown in Fig. 2 as if both sides of the actuator were fixed and had infinite impedance output loads. This case was often analyzed in high impedance test setting, in which both sides of the actuator are firmly fixed to the ground as shown in Fig. 3. The lumped model was considered valid for this setting only because the actuator inertia is constrained to move in a lumped manner due to the gear's no-slip condition [19]. However, in most situations, the output loads such as the upper body of the robot will be able to move, and torque will be transmitted directly to springs without gear rotation. This will make the lumped model invalid.

SEAs are often categorized by spring location as mentioned in [4]. For clarity, we will follow a similar notation throughout

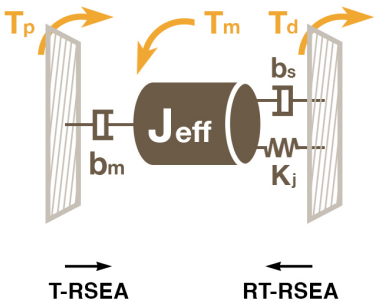

FIGURE 3. LUMPED MODEL SEA IN HIGH IMPEDANCE SETTING

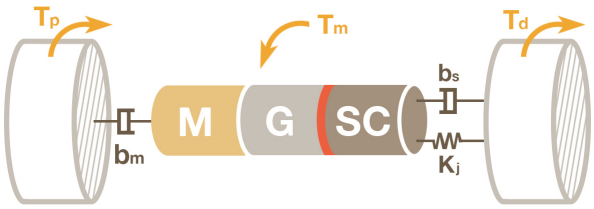

FIGURE 4. UNLUMPED MODEL SEA IN MOVING OUTPUT SETTING

the paper. We will call the actuator a T-RSEA (Torque sensing Rotary SEA) if the gear train is next to spring, and a RT-RSEA (Reaction Torque sensing Rotary SEA) if the motor housing is next to the spring as shown in Fig. 5.

However, as Orekhov claimed [22], this distinction has little significance when we consider both ends as possible outputs. This is clear when we consider the actuator as a traditional lumped model as in Fig. 3, where J_{eff} is the lumped inertia which combines the reflected inertia with the spring chassis inertia. As shown in Fig. 3, the actuator will operate in different modes depending on the direction of the applied torque. Note that the configuration does not change when the torque direction changes, but its functional characteristic changes. We will talk more in detail in section 3.1.3

2.2 Mechanical Impedance Analogy and Electrical Circuit Representation of Series Elastic Actuators

One way to gain additional insight into how SEAs behave is using the mechanical impedance analogy to represent mechanical parts as impedances in an electrical circuit. This method was first described by Schutz et. al in [21]. In this analogy, force (or torque) is analogous to voltage, and velocity (or angular velocity) is analogous to current. In this framework, each of the passive circuit elements from electrical circuits has a corresponding mechanical equivalent. These equivalents are shown in Table 1.

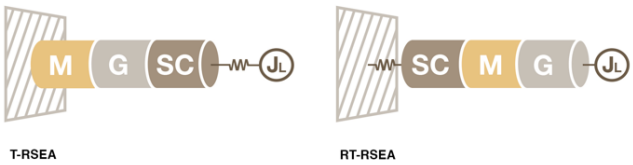

FIGURE 5. (a) TORQUE SENSING RSEA (b) REACTION TORQUE SENSING RSEA

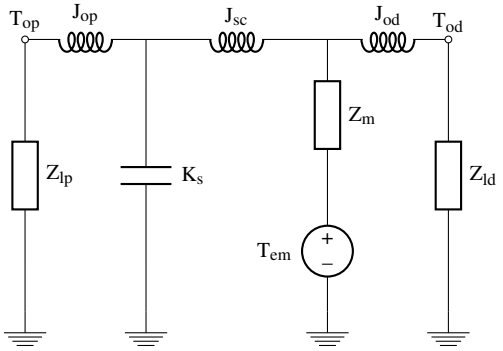

FIGURE 6. ELECTRICAL CIRCUIT MODEL OF SEA

At junctions, the sum of the motions should be equal to zero. Likewise the sum of forces in a loop from one junction to another must be zero. Additionally, among elements in parallel, the force distributed among them must be the same. These are the "duals" of Kirchoff's laws that state that the sum of currents into a node equals zero and that the sum of voltages in a loop must be equal to zero. We can derive the electrical dual circuit in Fig. 6 from the mechanical model in Fig. 4. In the figure, elements labeled with a "Z" represent the combined impedance of a capacitor, inductor and resistor together. Detailed derivation steps are shown in [21].

Fig. 6 shows the general case of output loads with finite

TABLE 1. Corresponding Mechanical and Electrical Impedances

Mechanical	Impedance	Electrical
Stiffness	K/s — 1/(Cs)	Capacitance
Rotary Inertia	Js — Ls	Inductance
Damping	B — R	Resistance
Gears	N^2 — Mu^2	Transformer

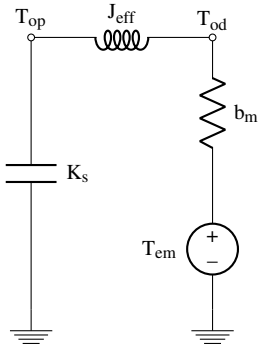

FIGURE 7. LUMPED MODEL HIGH IMPEDANCE CIRCUIT

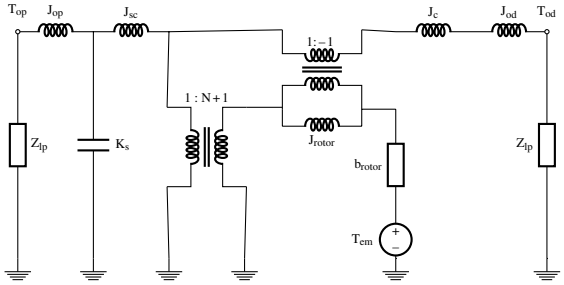

FIGURE 8. ELECTRICAL CIRCUIT MODEL OF T-RSEA WITH EPICYCLIC GEAR TRAIN

impedance. To see the limiting case with infinite impedance, we remove the output branches and replace them with a short circuit as in Fig. 7. Note that the reflected inertia of the rotor is forced to move with the output load, and is lumped together in the same branch ($J_{eff} = J_{sc} + J_m$), meaning that the speed of the rotor and chassis must be equal. Since the chassis inertia is typically two to three orders of magnitude smaller than the reflected inertia of the rotor, the lumped impedance model overstates the influence of the reflected inertia on system dynamics.

An electrical circuit for an epicyclic gear train was first described by Schutz in [21]. In their work, they described an epicyclic gear train for an RT-RSEA. Since our actuator is a T-RSEA, we modified the diagram to be as follows, with a gear ratio of $Mu_1 = N + 1 = 502$ and $Mu_2 = -1$ to account for the Dynamixel Pro's stator-annulus coupling. We have explicitly included the gears as transformers in our diagram to illustrate the 3 port topology. With this setup, we can see that the rotor's effective impedance is different when viewed from the distal port versus the proximal port.

2.3 MODELING AND ACTUATOR DYNAMICS

In order to analyze the input-output relationships between the motor and the proximal and distal loads, we need the transfer functions T_d/T_m, T_p/T_m, and T_d/T_p for both the lumped case and the unlumped case. Note that the following transfer functions were derived for a Torque sensing Rotary SEA.

2.3.1 High Impedance Lumped and Unlumped Transfer Functions In the high impedance case, Z_{ld} and Z_{lp} in Fig. 6 are considered to have infinite impedance and the mechanical schematic of the system looks like Fig. 3. In this case, the transfer function (1) and (2) can be derived either from free body diagrams of Fig. 3 or from the electrical circuit in Fig. 6. Note that we define the effective viscosity as $b_{eff} = b_m + b_s$ where $b_m = b_{rotor} \times N^2$ and b_s is the spring viscosity and N is the gear ratio.

$$\frac{T_d(s)}{T_m(s)} = \frac{K_s}{J_{eff}s^2 + b_{eff}s + K_s} \tag{1}$$

$$\frac{T_p(s)}{T_m(s)} = \frac{J_{eff}s^2 + b_s s + K_s}{J_{eff}s^2 + b_{eff}s + K_s} \tag{2}$$

Dividing equations (1) and (2) yields the end-to-end transfer function as in Eqn. (3)

$$\frac{T_d(s)}{T_p(s)} = \frac{K_s}{J_{eff}s^2 + b_s s + K_s} \tag{3}$$

Here, we should note that the denominator of the transfer function contains the lumped inertia. In contrast, the unlumped model has transfer functions:

$$\frac{T_d(s)}{T_m(s)} = \frac{K_s}{(J_{rotor} \cdot N^2 + J_{sc})s^2 + (b_m \cdot N^2 + b_s)s + K_s} \tag{4}$$

$$\frac{T_p(s)}{T_m(s)} = \frac{J_{sc}s^2 + b_s s + K_s}{(J_{rotor} \cdot N^2 + J_{sc})s^2 + (b_m \cdot N^2 + b_s)s + K_s} \tag{5}$$

$$\frac{T_d(s)}{T_p(s)} = \frac{K_s}{J_{sc}s^2 + b_s s + K_s} \tag{6}$$

Note that T_d/T_m is identical for the lumped and unlumped models (Eqn. (1) and (4)) due to the no slip condition. When

both ends are fixed, the gear is forced to move with the spring chassis under loading. As Orekhov pointed out, this is why the lumped model has been considered a legitimate representation of SEAs for a long time by many researchers.

However, when we consider the end-to-end transfer function from T_p to T_d, we can see that the two transfer functions are significantly different since the unlumped model does not contain the reflected inertia term.

As long as Eqn. (6) has a magnitude of unity, the internal dynamics of the actuator are negligible and the actuator can be considered a pure torque source by other actuators. In other words, provided that the actuator operates below the bandwidth frequency which can be calculated from Eqn. (7), the actuator can be considered a pure torque source with the potential for high force fidelity.

2.3.2 Moving Output Simulation In order to observe the unlumped model behavior from the transfer function analysis, we want to observe the frequency response T_p/T_m and T_d/T_m. However, such an experiment requires an additional F/T sensor attached on the other end. Instead, we noted that the unlumped model can also be observed from a moving output test, in which one or both ends of the actuator have finite impedance so that they are left free to rotate as shown in Fig. 4. This is a better representation of the actual model since in reality, the distal link of the actuator is fixed to the ground while the proximal load has finite impedance during the single support phase as shown in Fig. 2. In this case, when torque is applied from proximal to distal link, the gear is not likely to rotate due to high reflected inertia, but the actuator itself moves without gear rotation, and torque is directly transmitted to the spring through the actuator body. In order to simulate the unlumped model, we created a model of the system in Simulink using the Power Systems module to predict the theoretical response of each of the systems and used the Linear Analysis toolbox to compute their frequency response. System parameters were either extracted through system identification or measured directly as described in Section 3.2.

2.4 Actuator Bandwidth

It is insightful to consider the bandwidth of the actuator to be considered a function of the spring stiffness and effective inertia. The unlumped model end-to-end transfer function shown in Eqn. (6) can be used to show this relationship. In other words, the natural frequency of the actuator can be calculated from Eqn. (6), which leads to the upper limit bandwidth frequency imposed solely by hardware.

In order to give a margin of safety before reaching the resonant frequency, a magnitude of 3 dB in the frequency response was chosen to correspond to the bandwidth frequency as shown in Eqn. (7).

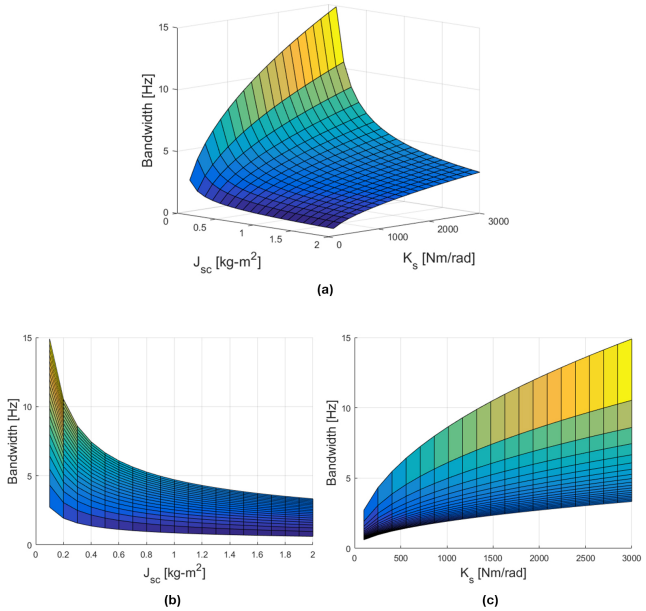

FIGURE 9. 3D MANIFOLD GRAPH (a) BANDWIDTH VS INERTIA VS STIFFNESS (b) BANDWIDTH VS INERTIA (c) BANDWIDTH VS STIFFNESS

As Orekhov stated in [22], the bandwidth frequency calculated from Eqn. (7) is based on the pure torque assumption since the transfer function shown in Eqn. (6) only considers torques being applied on either end of the actuator.

In other words, the Eqn. (7) gives a theoretical bandwidth frequency up to where the pure torque assumption is valid for Rotary SEAs. If the actuator performs above this frequency range, the internal dynamics of the actuator take effect, and the actuator cannot be considered a pure torque source. In other words, as long as the actuator is controlled within the operational bandwidth given by the Eqn. (7), the internal dynamics are negligible and the actuator can be treated as a pure torque source. This will lift the computational burden on higher level controllers significantly.

$$\text{Bandwidth} = \frac{1}{2\pi}\sqrt{\frac{.292K_s}{J_{sc}}} \tag{7}$$

Further note that a similar equation can also be derived from Eqn. (3). This implies that the bandwidth criteria is applicable for all inertia values regardless of the actuator model. Although Eqn. (7) ignores some of the subtleties of actuator dynamics, it clearly shows the two ways to increase actuator bandwidth. 1) Increase the spring stiffness, at the cost of losing compliance. 2)

Decrease the effective inertia of the system.

As can be seen from the Fig. 9, the surface is not linear. Hence, there are some engineering tradeoffs that can be made in terms of spring stiffness and inertia in order to gain vastly improved open loop bandwidth. In other words, one can attain a wide range of stiffness variation within the allowed frequency range by making the spring chassis inertia significantly small. Eqn. (7) is a compact and powerful way of encapsulating the relationship between stiffness and inertia in this regard.

3. EXPERIMENTAL VALIDATION

3.1 Test Platform Setup

To validate our methodology, we designed and built a T-RSEA shown in Fig. 10 to serve as a test platform for assessing the effect of changing the stiffness and inertia settings for the actuator. The elastic element is two pairs of opposing linear springs arranged so as to provide torsional compliance. Fixed spring constant with an adjustable moment arm mechanism shown in [17] was utilized as shown in Fig. 11.

3.1.1 Specifications A picture of the completed actuator is shown in Fig. 10. The motor is a 24V, 200W Dynamixel Pro H54-200-S500-R robot actuator from Robotis. The Dynamixel has a 502:1 gear ratio with a maximum continuous torque output of 44.2 N-m and a no-load speed of 33.1 RPM. To sense torque, we used the ATI Mini58 6-axis force/torque sensor that is rigidly mounted to the end of the actuator. An absolute encoder is mounted on the actuator but it was not utilized for this experiment.

3.1.2 Desired Characteristics and Mechanism Analysis In order to use the linear relationship $T = -k\vartheta$ for the springs, joint stiffness should be constant throughout the deflection. In order to achieve these characteristics with a set of linear springs, the test platform was designed to deflect less than 5 degrees in either direction to minimize the effect of spring buckling. Further, torque values were calculated from Eqn. (8) while joint stiffness values were calculated from Eqn. (9). These equations were obtained through the analysis steps shown in [9].

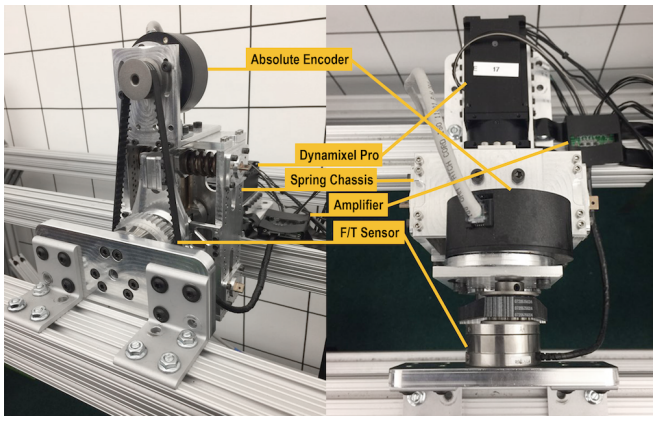

FIGURE 10. TORQUE SENSING ROTARY SEA TEST PLATFORM

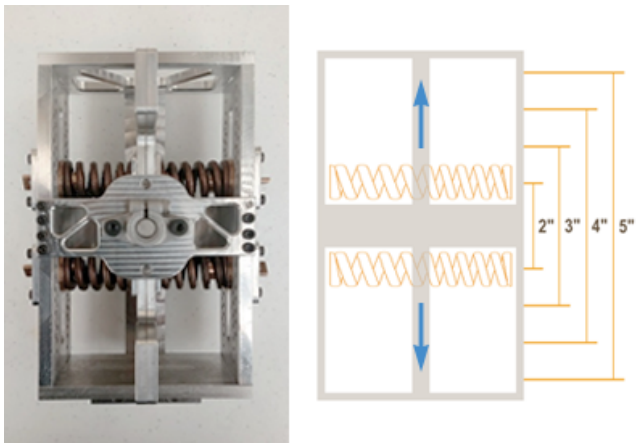

FIGURE 11. ADJUSTABLE JOINT STIFFNESS WITH VARYING MOMENT ARM

$$T = 2K(R^2 + \frac{r_s^2}{3})\sin\vartheta_s\cos\vartheta_s \tag{8}$$

$$K_s = 2K(R^2 + \frac{r_s^2}{3})(2\cos^2\vartheta_s - 1) \tag{9}$$

3.1.3 Moving Output Test Configuration for T-RSEA As explained in Section 2.1, the distinction between torque(force) sensing and reaction torque(force) sensing actuators has little significance. However, all the relevant works [4,19,21] were based on the Reaction Force sensing linear Series Elastic Actuators. Since our work is based on a Torque sensing Rotary Series Elastic Actuator, we will show the difference in configuration and examine its validity when a torque sensing actuator is used as a reaction torque sensing actuator.

As shown in Fig. 12, when a torque sensing actuator acts like a reaction torque sensing actuator due to the output impedance change, its configuration becomes similar to the conventional RT-RSEA shown in Fig. 5 (b), except that the motor and gear locations are now swapped. This change in configuration has little effect on the actuator performance especially when the gear ratio is high. The distinction between the RT-RSEA and T-RSEA

FIGURE 12. T-RSEA IN MOVING OUTPUT TEST SETTING

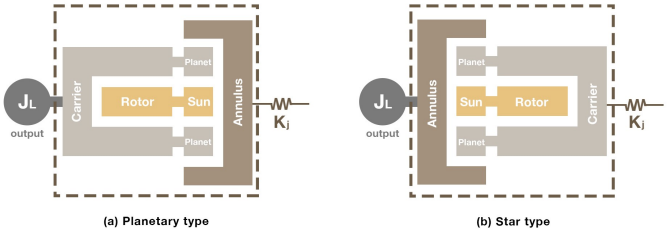

FIGURE 13. PLANETARY GEAR REPRESENTATIONS OF RSEA IN MOVING OUTPUT TEST

is important especially if the impedance, J_c, is close in value to the reflected inertia, J_m. However, for the case in which the gear ratio is large, the effect of the reflected inertia outweighs the difference from changing the position of J_c.

Since many humanoid robots that use SEAs require high torque, harmonic drives are widely used as a reduction mechanism in many rotary form SEAs. On the other hand, the Dynamixel Pro motor in our test equipment uses a cycloidal gear train. Since a planetary gear train shares the same fundamental mechanism and can be used to describe both Harmonic drive and cycloidal gear trains, we show the difference in configuration using the planetary gear train as shown in Fig. 13

The cycloidal gear train in the Dynamixel Pro motor has stator-annulus coupling, which means that the stator is attached to the annulus of the motor. Fig. 13 (a) shows a configuration of a planetary gear train in a conventional reaction torque sensing actuator, where the output load is connected to a carrier-planetary gear pair. On the other hand, in a case where the torque(force) sensing actuator is used as a reaction torque(force) sensing actuator, the output load is attached to the annulus while the carrier-planetary gear pair is connected to the spring. Fig. 13 (a) is often called the planetary type having a gear ratio of N+1, whereas Fig. 13 (b) is called the star type having a gear ratio of -N. Since the gear ratio of the Dynamixel Pro motor is significantly high, the effect of the ratio change is rather small. A more significant change is the added motor inertia to an output load, which is also significantly smaller than the inertia produced by the output link.

3.2 System Identification

In order to find parameters for the end-to-end transfer function, we experimentally determined the system's parameters using the system identification methods. We used the Dynamixel's torque mode, which sends current input with feed-forward constant, to command output torques. The force/torque sensor attached at the end of the spring measured the output torque, T_d, directly. For all tests, the torque response was recorded at a sampling rate of 280 Hz.

3.2.1 High Impedance Test For the high impedance test, both ends of the actuator were firmly fixed to the test frame as shown in Fig. 14. The commanded reference signal was a sinusoidal chirp signal summed with noise signal. The noise signal was added to the reference signal to mitigate static friction in the gear train at low frequencies. The signal has an amplitude of 20 Nm and used a logarithmic sweep from 0.01 - 140 Hz over 160 seconds. The noise signal was Gaussian white noise with a standard deviation of 10 N and a frequency range from 0.01 Hz to 140 Hz. Stiffness setting of K_s=1,690.5 Nm/rad calculated from Eqn. (9) based on the nominal spring constant value, K= 207,350 N/m and 127 mm (5in) separation was used. Frequency response data was then fitted to a 2nd order transfer function to extract J_{eff} and b_{eff} values. The second order fitted transfer function is shown in (10) as an example. Two different K_s/J_{eff} values were averaged, then J_{eff}, and b_{eff} values were extracted using the measured joint stiffness value. The measured stiffness value was used instead of the calculated one since the nominal spring constant value provided by a manufacturer was not accurate and was also slightly different for each spring. The Table 2 lists all the parameter values used for simulation. Inertia values for each part of the test equipment were calculated from the model in SolidWorks. The reflected inertia value, J_m, was obtained after subtracting the spring chassis inertia, J_{sc} , from the extracted value,

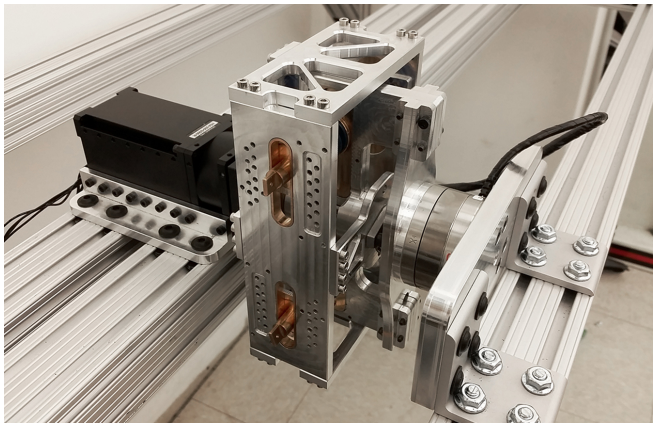

FIGURE 14. HIGH IMPEDANCE TEST SETTING

TABLE 2. ACTUATOR PARAMETER VALUES

Parameter	Value	Parameter	Value
J_{op}	0.0012 kgm^2	J_{od}	0.010 kgm^2
J_{lp}	1×10^8 kgm^2	J_{ld}	0.091 kgm^2
J_m	0.953 kgm^2	J_{sc}	0.0040 kgm^2
b_s	3 Nms	b_m	23.088 Nms
b_{lp}	1×10^8 Nms	b_{ld}	0.02 Nms
K_{lp}	1×10^8 Nm/rad	K_{ld}	7 Nm/rad
K_s	1530.456 Nm/rad		

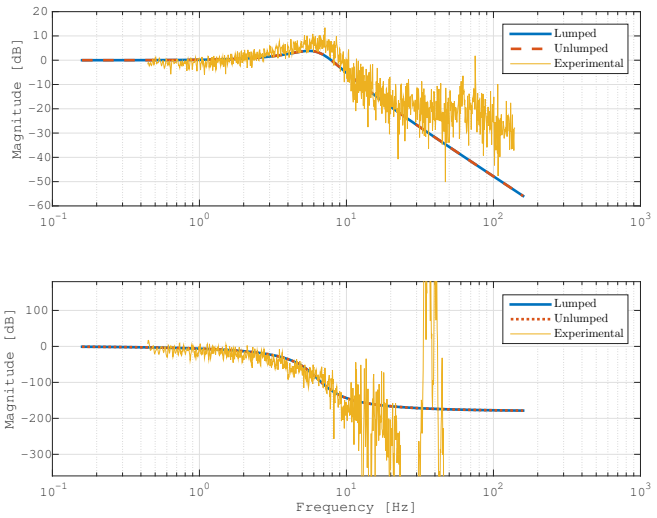

FIGURE 15. COMPARISON OF SYSTEM FREQUENCY RESPONSE T_d/T_m IN HIGH IMPEDANCE TEST

J_{eff}. Similarly, the reflected damping, b_m, was obtained after subtracting the spring damping, b_s, from the extracted value, b_{eff}. A few values such as K_{ld}, b_{ld}, and b_s were approximated.

$$\frac{\frac{K_s}{J_{eff}}}{s^2 + \frac{b_{eff}}{J_{eff}}s + \frac{K_s}{J_{eff}}} = \frac{1560.436}{s^2 + 27.267s + 1638.783} \tag{10}$$

Fig. 15 shows the high impedance bode plot of Torque sensing Rotary SEA which agrees with the case of the Reaction Force sensing linear SEA presented in [19]. As it can be clearly seen, the T_d/T_m transfer function alone cannot fully describe SEA characteristics since the unlumped model moves in the same manner as the lumped model when both ends are firmly fixed.

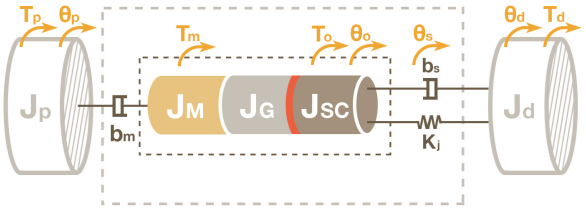

FIGURE 16. UNLUMPED MODEL SCHEMATIC WITH MOVING OUTPUTS

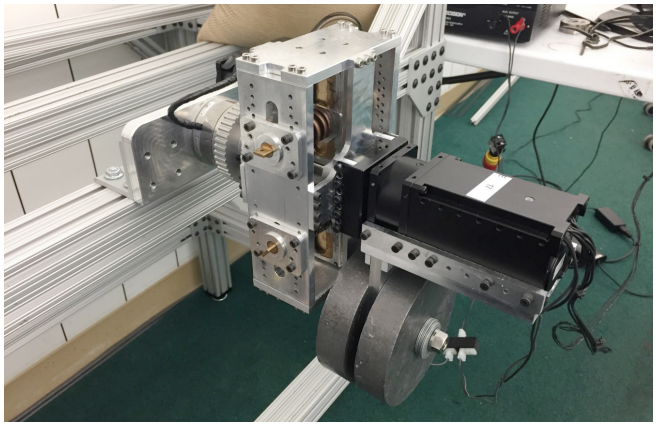

FIGURE 17. T-RSEA IN MOVING OUTPUT TEST CONFIGURATION

3.2.2 Moving Output Test Fig. 16 shows the most general case of the unlumped model in the moving output setting. If the inertia components inside the inner dashed line are combined, the system can be considered a lumped model. If the components inside the outer dashed line are used with infinite impedance on both ends, the system can be considered as in the high impedance test. The schematic as a whole represents the unlumped model having both ends as moving output. The system dynamics for the moving output test was simulated in Simulink using the equivalent electrical circuit model shown in Fig. 8.

For the actual moving output test, one end of the actuator (distal link) was left free to rotate while the other end was firmly fixed to the test frame as shown in Fig. 17. A pendulum of 5.8 kg weight with a 0.114 m (4.5 in) link was attached to the motor to simulate the inertia of an output link in humanoid robots. System identification was conducted with Gaussian white noise with a standard deviation of 30 N. The frequency range was from 0.01 Hz to 140 Hz and the sweeping time was 160 s. The noise only signal was used in this case to prevent the pendulum swinging at large angles. As it is evident in Fig. 18, the actuator response is

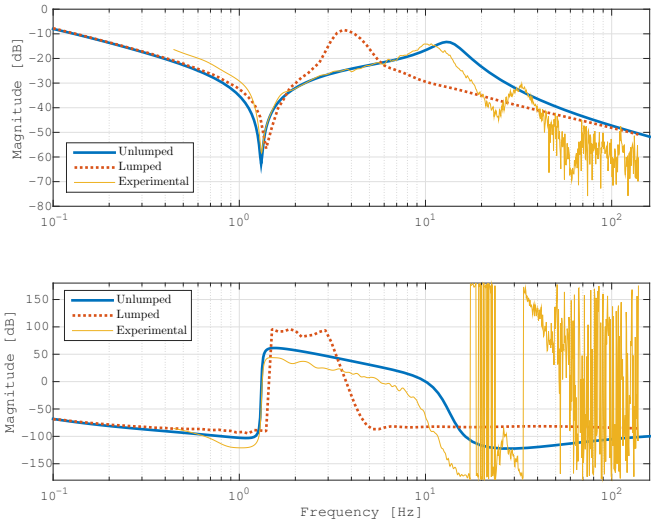

FIGURE 18. COMPARISON OF SYSTEM FREQUENCY RESPONSE T_p/T_m IN MOVING OUTPUT TEST

more closely approximated by the unlumped actuator model than the lumped model. The pendulum on the moving output side of the actuator was approximated by changing K_{ld} and b_s to have a resonance at the same frequency as the pendulum. Table 2 lists all the parameters used in the simulation. The resonance around 33 Hz is likely from an unmodeled resonance in the chassis of the actuator. A likely explanation for the discrepancy between the simulated model and the experimental results at higher frequencies is the actuator's out of plane oscillation which was a drawback of the planar spring box configuration. Around 19 Hz the experimental phase becomes out of sync with the actuator. We hypothesize that this was caused by the actuator output being very small relative to the signal to noise ratio of the torque sensor that we used. The combination of having noise as the only input and having relatively low amplitude oscillations likely decreased our signal-to-noise ratio. Nevertheless, the unlumped model demonstrates the ability to capture approximate system dynamics of the actuator much better than the lumped model.

4. IMPLICATIONS FOR SEA DESIGN

4.1 Prototype Design

Using Eqn. (7), we can make a Rotary SEA to achieve a target frequency. In order to fully explore the potential implication of this equation, a prototype design process will be elaborated. For example, if we are given a task to design a force controllable actuator for a human size robot to climb stairs, we first need to consider the required torque of the actuator in the lower body. As shown in [23], the required torque from a knee pitch actuator for a human size robot to climb the stairs is around 150 Nm.

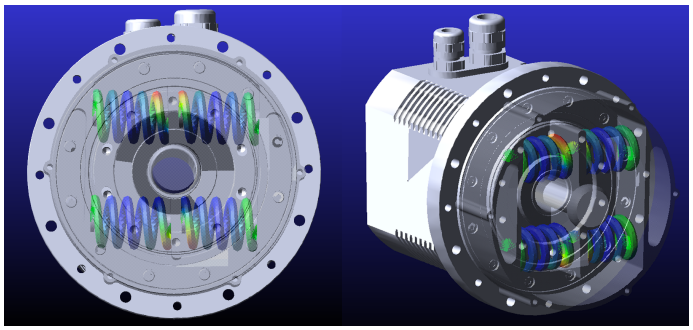

FIGURE 19. FEA ANALYSIS OF RSEA PROTOTYPE IN ADAMS

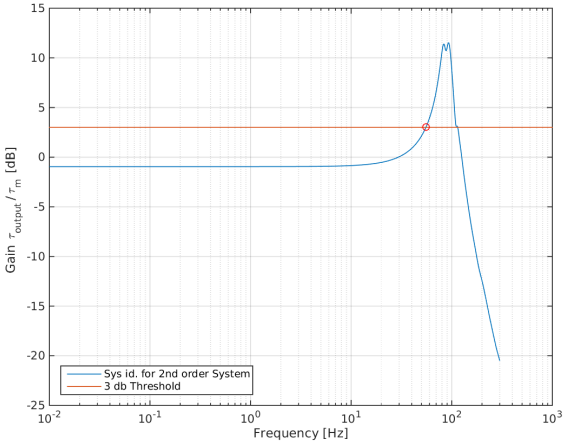

FIGURE 20. OPEN LOOP FORCE CONTROL RESPONSE FROM SIMULATION

In order to satisfy this requirement, Robodrive motor-gear unit RD85x13-HD was chosen. With the built-in 160:1 harmonic gear drive CPL-25A-160-2A, the motor-gear unit can produce a peak torque of 176 Nm, continuous torque of 67 Nm, and weighs 3.65 kg. Its outer diameter is 0.12 m, so the spring chassis was designed to have the same diameter but as light as possible to minimize the inertia. The designed spring chassis has a mass of 0.245 kg and a moment of inertia along the rotational axis of 6.169 e-04 kg-m^2. Further, since force controllable actuators are typically operated at bandwidths between 15-60 Hz [19], we set our target frequency to be above 50 Hz. The spring stiffness value was chosen based on the target bandwidth and Eqn. (9). The spring was designed after a few iterations of FEA in ADAMS to have a value of 185,185 N/m, making the torsional stiffness value of 260 Nm/rad with 0.0508 m (2 in) separation between springs as shown in Fig. 19. Finally, open loop force control was simulated based on the unlumped model of the actuator. The simulated bode plot shown in Fig. 20 revealed that it can achieve a band-

width frequency value of 55.5 Hz, meaning that the actuator can be considered as a pure torque source up to this frequency despite its high gear ratio and relatively heavy weight. As long as the actuator is considered a pure torque source, high fidelity force control is possible.

5. CONCLUSION

In order to verify that the unlumped models is a valid representation of Rotary SEAs, we performed a series of experiments to test the system's validity.

The high impedance test demonstrated that the unlumped model performs similarly to the lumped model when the gear is constrained to move due to no-slip condition. On the other hand, the moving output test showed that the unlumped model peforms differently from the lumped model, accurately depicting the motor to distal output frequency response. System identification of the actuator and simulation of the SEA using an unlumped and lumped SEA model verified that the unlumped model is a more accurate description than the lumped model when one of the output loads has a finite impedance, which, in reality, is a better representation of actuator dynamics.

We further developed our analysis of the factors that influence the force control bandwidth. We concluded that there are definite ways to maximize the compliance of a RSEA given a task requiring a specific torque and force control bandwidth.

We concluded with an example of our design methodology for design of a RSEA and verified through simulation that the actuator has the desired output force bandwidth.

6. FUTURE WORK

Future work could include a multiple moving output test with two outputs as in [24], building the high bandwidth actuator described in section 4, and implementing control systems for such an actuator. Another avenue of research would be to develop an actuator with separate stiffnesses for the proximal and distal loads.

ACKNOWLEDGMENT

Thanks to all of our labmates past and current at RoMeLa for all of your support, ideas and thoughtful suggestions. A special thanks to Taoyuanmin Zhu and Benson Ku for assisting with LabVIEW and helping to set up our experimental apparatus. An additional thanks to Steffen Schutz, Atabak Nejadfard and the rest of the RRLAB at University of Kaiserslautern, whose correspondence and input greatly enhanced this work. Last but not least, we would like to thank Sun-A Shin for making beautiful images throughout the paper.

We would also like to acknowledge our gratitude to the Office of Naval Research, through whom this research was funded and made possible. This work was supported by ONR Award Number N00014-15-1-2064.

REFERENCES

[1] Pratt, G., and Williamson, M., 2000. "Series Elastic Actuators". *Proceedings 1995 IEEE/RSJ International Conference on Intelligent Robots and Systems. Human Robot Interaction and Cooperative Robots*.

[2] Knabe, C., Lee, B., Orekhov, V., and Hong, D., 2014. "Design of a Compact, Lightweight, Electromechanical Linear Series Elastic Actuator". *Volume 5B: 38th Mechanisms and Robotics Conference*.

[3] Pratt, J., Krupp, B., and Morse, C., 2002. "Series elastic actuators for high fidelity force control". *Industrial Robot: An International Journal,* ***29***(3), p. 234241.

[4] Paine, N., Oh, S., and Sentis, L., 2014. "Design and Control Considerations for High-Performance Series Elastic Actuators". *IEEE/ASME Transactions on Mechatronics,* ***19***(3), p. 10801091.

[5] Orekhov, V., Lahr, D., Lee, B., and Hong, D., 2013. "Configurable Compliance for Series Elastic Actuators". *Volume 6B: 37th Mechanisms and Robotics Conference*, Apr.

[6] Lee, B., Knabe, C., Orekhov, V., and Hong, D., 2014. "Design of a Human-Like Range of Motion Hip Joint for Humanoid Robots". *Volume 5B: 38th Mechanisms and Robotics Conference*.

[7] Pratt, J., and Krupp, B., 2008. "Design of a bipedal walking robot". *Unmanned Systems Technology X*, Mar.

[8] Paine, N., Mehling, J. S., Holley, J., Radford, N. A., Johnson, G., Fok, C.-L., and Sentis, L., 2015. "Actuator Control for the NASA-JSC Valkyrie Humanoid Robot: A Decoupled Dynamics Approach for Torque Control of Series Elastic Robots". *Journal of Field Robotics,* ***32***(3), p. 378396.

[9] Tsagarakis, N., Laffranchi, M., Vanderborght, B., and Caldwell, D., 2009. "A compact soft actuator unit for small scale human friendly robots". *2009 IEEE International Conference on Robotics and Automation*.

[10] Tsagarakis, N. G., Morfey, S., Cerda, G. M., Zhibin, L., and Caldwell, D. G., 2013. "COMpliant huMANoid COMAN: Optimal joint stiffness tuning for modal frequency control". *2013 IEEE International Conference on Robotics and Automation*.

[11] Negrello, F., Garabini, M., Catalano, M. G., Malzahn, J., Caldwell, D. G., Bicchi, A., and Tsagarakis, N. G., 2015. "A modular compliant actuator for emerging high performance and fall-resilient humanoids". *2015 IEEE-RAS 15th International Conference on Humanoid Robots (Humanoids)*.

[12] Englsberger, J., Werner, A., Ott, C., Henze, B., Roa, M. A., Garofalo, G., Burger, R., Beyer, A., Eiberger, O., Schmid,

K., and et al., 2014. "Overview of the torque-controlled humanoid robot TORO". *2014 IEEE-RAS International Conference on Humanoid Robots*.

[13] Kim, J., Lee, Y., Kwon, S., Seo, K., Kwak, H., Lee, H., and Roh, K., 2012. "Development of the lower limbs for a humanoid robot". *2012 IEEE/RSJ International Conference on Intelligent Robots and Systems*.

[14] Hobbelen, D., Boer, T. D., and Wisse, M., 2008. "System overview of bipedal robots Flame and TUlip: Tailor-made for Limit Cycle Walking". *2008 IEEE/RSJ International Conference on Intelligent Robots and Systems*.

[15] Hurst, J. W., Chestnutt, J. E., and Rizzi, A. A., 2010. "The Actuator With Mechanically Adjustable Series Compliance". *IEEE Transactions on Robotics,* ***26***(4), p. 597606.

[16] Tsagarakis, N. G., Sardellitti, I., and Caldwell, D. G., 2011. "A new variable stiffness actuator (CompAct-VSA): Design and modelling". *2011 IEEE/RSJ International Conference on Intelligent Robots and Systems*.

[17] Jafari, A., Tsagarakis, N. G., and Caldwell, D. G., 2013. "A Novel Intrinsically Energy Efficient Actuator With Adjustable Stiffness (AwAS)". *IEEE/ASME Transactions on Mechatronics,* ***18***(1), p. 355365.

[18] Wolf, S., Eiberger, O., and Hirzinger, G., 2011. "The DLR FSJ: Energy based design of a variable stiffness joint". *2011 IEEE International Conference on Robotics and Automation*.

[19] Orekhov, V. L., Knabe, C. S., Hopkins, M. A., and Hong, D. W., 2015. "An unlumped model for linear series elastic actuators with ball screw drives". *2015 IEEE/RSJ International Conference on Intelligent Robots and Systems (IROS)*.

[20] Robinson, D. W., 2000. "Design and analysis of series elasticity in closed-loop actuator force control". PhD thesis, Massachusetts Institute of Technology, Cambridge, MA, June.

[21] Schutz, S., Nejadfard, A., Kotting, C., and Berns, K., 2016. "An intuitive and comprehensive two-load model for Series Elastic Actuators". *2016 IEEE 14th International Workshop on Advanced Motion Control (AMC)*.

[22] Orekhov, V., 2014. "Series elasticity in linearly actuated humanoids". PhD thesis, Virginia Polytechnic Institute and State University, Blacksburg, VA, Dec.

[23] Knabe, C., Seminatore, J., Webb, J., Hopkins, M., Furukawa, T., Leonessa, A., and Lattimer, B., 2015. "Design of a series elastic humanoid for the DARPA Robotics Challenge". *2015 IEEE-RAS 15th International Conference on Humanoid Robots (Humanoids)*.

[24] Schutz, S., Mianowski, K., Kotting, C., Nejadfard, A., Reichardt, M., and Berns, K., 2016. "Rrlab sea a highly integrated compliant actuator with minimised reflected inertia". *2016 IEEE International Conference on Advanced Intelligent Mechatronics (AIM)*.